

Thermal receptivity of free convective flow from a heated vertical surface: Linear waves

Manosh C. Paul^{a,*}, D. Andrew S. Rees^b, Michael Wilson^b

^a *Department of Mechanical Engineering, University of Glasgow, Glasgow G12 8QQ, UK*

^b *Department of Mechanical Engineering, University of Bath, Bath BA2 7AY, UK*

Received 14 June 2006; received in revised form 18 July 2007; accepted 26 October 2007

Available online 9 January 2008

Abstract

Numerical techniques are used to study the receptivity to small-amplitude thermal disturbances of the boundary layer flow of air which is induced by a heated vertical flat plate. The fully elliptic nonlinear, time-dependent Navier–Stokes and energy equations are first solved to determine the steady state boundary-layer flow, while a linearised version of the same code is used to determine the stability characteristics. In particular we investigate (i) the ultimate fate of a localised thermal disturbance placed in the region near the leading edge and (ii) the effect of small-scale surface temperature oscillations as means of understanding the stability characteristics of the boundary layer. We show that there is a favoured frequency of excitation for the time-periodic disturbance which maximises the local response in terms of the local rate of heat transfer. However the magnitude of the favoured frequency depends on precisely how far from the leading edge the local response is measured. We also find that the instability is advective in nature and that the response of the boundary layer consists of a starting transient which eventually leaves the computational domain, leaving behind the large-time time-periodic asymptotic state. Our detailed numerical results are compared with those obtained using parallel flow theory.

© 2007 Elsevier Masson SAS. All rights reserved.

Keywords: Linear instability; Thermal receptivity; Free convection; Boundary layer

1. Introduction

The general problem of stability of free convective boundary layer flows is a combination of the problems of hydrodynamic instability and thermo-convective instability. Thermo-convective instabilities arise in cases where less dense fluid lies under more dense fluid. Examples of such situations include the classical Bénard convection problem, and boundary layer flows over inclined heated surfaces. For the latter example the primary mode of instability takes the form of longitudinal vortices in the direction of the induced basic flow (see Haaland and Sparrow [1] and Chen and Tzuoo [2]). On the other hand, for free convection boundary layer flow over a vertical heated surface, buoyancy forces generate the basic flow, but the primary instability is known to be hydrodynamic in origin. In this

case, the primary mode of instability takes the form of two-dimensional waves travelling in the streamwise direction (see Nachtsheim [3] and Heiber and Gebhart [4]).

In studies of instabilities, a small disturbance is often imposed onto the basic flow in order to assess the stability and transition processes inside the boundary layer. The classical mechanism by which imposed disturbances are converted into Tollmien–Schlichting (TS) type waves is known as the receptivity of the boundary layer. The term ‘receptivity’ was first introduced by Morkovin [5] to evaluate the transition process from laminar to turbulent flows.

The boundary layer flow stability problems with receptivity are usually classified into two categories. One is the study of receptivity to external disturbances which are naturally present in the ambient environment, e.g. acoustic and vortical perturbations in the ambient fluid and surface roughness over which a fluid flow generates disturbance waves into the flow. Some relevant published works to this category are Goldstein [6,7], Dietz [8], Wu [9–11], Tam [12], Haddad and Corke [13],

* Corresponding author. Tel.: +44 (0) 141 330 8466; fax: +44 (0) 141 330 4343.

E-mail address: m.paul@mech.gla.ac.uk (M.C. Paul).

Nomenclature

a	scaling factor	ϕ	angular coordinate
f, h	basic boundary layer solutions	ψ	streamfunction
F	buffer function	ω	vorticity
g	gravitational acceleration	ξ, η	similarity variables
Pr	Prandtl number		
k	spatial wavenumber	<i>Subscripts</i>	
L	spatial wavelength	$b1$	start of buffer region
Q	surface rate of heat transfer	$b2$	end of buffer region
M	maximum value of $ Q $	DIST	disturbance
t	time	max	maximum value
T	temperature of fluid	min	minimum value
u, v	fluid velocities in x and y directions respectively	new	present iteration value
x, y	nondimensional Cartesian coordinates	old	previous iteration value
		opt	optimum value
<i>Greek symbols</i>			
β	coefficient of thermal expansion	<i>Superscripts</i>	
χ	vorticity or temperature in Eq. (29)	'	derivatives with respect to η
λ	temporal frequency	—	steady flow quantities
ν	fluid viscosity	^	perturbation flow quantities
θ	nondimensional temperature		

and the references therein. The second category concerns the study of receptivity to spatially localised disturbances which are introduced within the boundary layer of a flow, e.g. suction/blowing slots and temperature perturbations generate disturbance waves inside boundary layer. Some relevant works to this category are Fasel and Konzelmann [14], Brooker et al. [15], Herwig and You [16].

The receptivity process considered in the present study belongs to the second category. We have considered a thermal receptivity process by which various external temperature disturbances are introduced into the free convection boundary layer flow near the leading edge of the vertical flat plate. The two-dimensional TS waves generated then grow or decay in accordance with an approximate linear stability theory described in Paul et al. [17]. But once the flow has settled and transients have travelled out of the computational domain, it is possible to determine how the amplitude of the disturbance (as given, say, by the maximum heat transfer over one period) varies with both streamwise direction x , and the disturbance frequency λ . The resulting neutral curve may then be compared with the parallel flow theory.

Our understanding of the receptivity process and the crucial mechanisms required for the generation of instability waves have largely come from the papers by Goldstein [6,7]. His works have been focused on localised disturbances either from the leading edge ([6]) or from changes in the wall geometry ([7]) which includes local surface roughness. Goldstein [6] also recognised that three general classes of receptivity regions might exist: (i) the leading-edge region where the basic boundary layer is thinner and grows rapidly, and the motion is governed by the unsteady boundary layer equation, (ii) regions which are much further downstream where the boundary layer is forced to make a rapid adjustment, and the motion is

governed by the Orr–Sommerfeld equation, and finally (iii) an overlap region where the TS wave solutions of regions 1 and 2 match asymptotically.

Although we have not performed an asymptotic analysis in the present paper, we have found that the results obtained from the parallel flow approximation study of Orr–Sommerfeld type undertaken by Paul et al. [17] are in excellent agreement with those of the present fully elliptic simulation at large streamwise distances from the leading edge. On the other hand there is a poor agreement between the results obtained from the two different methods at locations near to the leading edge. Thus it is shown that the full elliptic system should be used, at least for this type of flow, rather than the parallel flow approximation.

So the general aim of this paper is to perform a numerical investigation to study the instability and receptivity of the thermal boundary layer flow over a vertical surface by introducing two different types of thermal disturbance into the steady flow: (i) an isolated internal disturbance, and (ii) time-periodic thermal disturbances. We use air as the working fluid and set the Prandtl number to 0.7. The thermal disturbances into the free convective flow are convectively unstable, as the generated two-dimensional waves travel to the downstream leaving behind the undisturbed solutions. The receptivity mechanism is a relevant issue for a convectively unstable flow. But, in some situations absolute instability may arise, e.g. when a surface temperature gradient is imposed (see Tao et al. [18]).

The literature is very limited on the study of the thermal receptivity and instability of a free convective boundary layer flow. To the authors' knowledge, there appears to be no full numerical investigation of such of the thermal boundary layer flow over a vertical heated surface. When the vertical thermal boundary layer is subject to harmonic disturbances in time, it is not clear how the strength of the subsequent response depends

on the frequency of the disturbance, whether there appears to be a most dangerous frequency in terms of the strength of the overall response which could maximise the boundary layer response, and how the frequency of the thermal disturbance will vary with the boundary layer thickness.

Our principal motivation of this study is to search for answers to the above hidden questions. Possible practical engineering applications fit within the range of industrial applications where a sudden or periodic change in the surface temperature can cause significant changes in the heat transfer process driven by the free convection. Moreover the thermal receptivity of the free convective boundary layer flows is of particular interest to the Thermofluid communities because the presence of an advectively unstable boundary layer means that the heat transfer may be increased substantially by the simple expedient of introducing a small oscillatory disturbance.

2. Equations of motion and boundary conditions

2.1. Governing equations

We consider the two-dimensional free convective boundary layer flow from a vertical semi-infinite heated plate. A schematic diagram of the flow domain showing the coordinate directions, the transformed coordinates and the boundary conditions is shown in Fig. 1. A Cartesian frame of reference is chosen, where the \bar{x} -axis is aligned vertically upwards

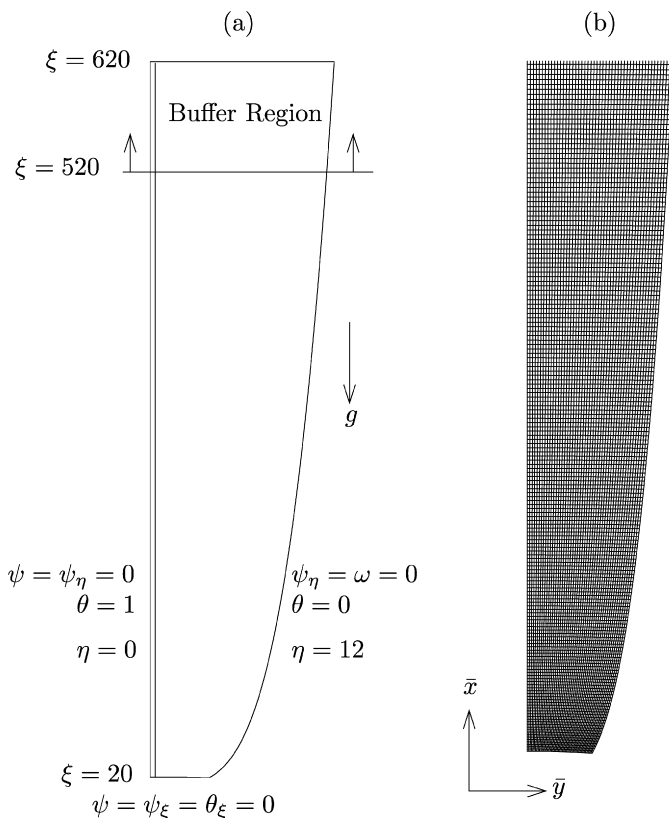


Fig. 1. (a) A schematic diagram of the flow configuration showing the coordinate directions and boundary conditions, (b) computational mesh. Note that the horizontal coordinate has been stretched greatly in this diagram.

with the heated surface. Convective flow is assumed to be governed by the equation of continuity, the incompressible Navier–Stokes equations and the energy transport equation subject to the Oberbeck–Boussinesq approximation. For unsteady two dimensional flow this system may be written in nondimensional streamfunction, vorticity and temperature form,

$$\nabla^2 \psi = \omega \tag{1}$$

$$\omega_t = \nabla^2 \omega + \psi_x \omega_y - \psi_y \omega_x + \theta_y \tag{2}$$

$$\theta_t = Pr^{-1} \nabla^2 \theta + \psi_x \theta_y - \psi_y \theta_x \tag{3}$$

(Paul et al. [17]) where $Pr = 0.7$ is the Prandtl number for air and the streamfunction is defined in the usual way according to $u = \psi_y$, $v = -\psi_x$ where u and v are the nondimensional fluid velocity components along the nondimensional coordinate directions x and y respectively.

It is important to note that our scalings do not give rise to a Grashof number in the governing nondimensional equations. That this is acceptable follows from the fact that there is no externally defined length scale in the idealised configuration being studied, and that the natural lengthscale $d = (v^2/g\beta\Delta T)^{1/3}$ is equivalent to setting the usual Grashof number to unity; such a procedure has also been used in studies of vortex disturbances in thermal boundary layer flows in porous media undertaken by Rees ([19,20]) where the governing Darcy–Rayleigh number was set to unity in order to define a natural lengthscale.

2.2. Coordinate transformation

The usual boundary layer approximation to Eqs. (1)–(3) is satisfied by the self-similar solutions

$$\psi = x^{3/4} f(\eta), \quad \theta = h(\eta), \quad \omega = x^{1/4} f''(\eta) \tag{4}$$

(see Pohlhausen [21] and Ostrach [22]) where $\eta = y/x^{1/4}$ is the similarity variable and where the functions f and h satisfy the ordinary differential equations,

$$f''' + \frac{3}{4} f f'' - \frac{1}{2} f' f' + h = 0 \tag{5}$$

$$h'' + \frac{3}{4} Pr f h' = 0 \tag{6}$$

subject to the boundary conditions

$$f(0) = f'(0) = h(0) - 1 = 0 \quad \text{and} \quad f', h \rightarrow 0 \quad \text{as } \eta \rightarrow \infty \tag{7}$$

This form of the similarity variable motivates the use of the Schwartz–Christoffel transformation

$$\left[\frac{3}{4} (\xi + i\eta) \right]^4 = (x + iy)^3 \tag{8}$$

which we use because it guarantees an orthogonal grid and thereby optimises the iterative numerical solution of Poisson equations such as (1). In polar coordinates, the transformation may be written in the form,

$$\xi = \frac{4}{3} r^{3/4} \cos \frac{3}{4} \phi, \quad \eta = \frac{4}{3} r^{3/4} \sin \frac{3}{4} \phi \tag{9}$$

where r is the nondimensional radial distance from the origin and ϕ is the angle from the upward vertical. In terms of ξ and η , Eqs. (1) to (3) become

$$\psi_{\xi\xi} + \psi_{\eta\eta} = A\omega \tag{10}$$

$$A\omega_t = \omega_{\xi\xi} + \omega_{\eta\eta} + \psi_{\xi}\omega_{\eta} - \psi_{\eta}\omega_{\xi} + A^{1/2}\left(\theta_{\xi}\sin\frac{1}{4}\phi + \theta_{\eta}\cos\frac{1}{4}\phi\right) \tag{11}$$

$$A\theta_t = Pr^{-1}(\theta_{\xi\xi} + \theta_{\eta\eta}) + \psi_{\xi}\theta_{\eta} - \psi_{\eta}\theta_{\xi} \tag{12}$$

where the function, A , is given by

$$A(\xi, \eta) = \left(\frac{3}{4}\right)^{2/3} (\xi^2 + \eta^2)^{1/3} \tag{13}$$

We note that it is not possible to write these equations solely in terms of ξ and η , but the ϕ -dependent terms in (11) may be computed easily using the definitions of ξ and η in Eq. (9).

2.3. Boundary conditions

The corresponding boundary conditions to be used to solve Eqs. (10)–(12) are

$$\psi = \psi_{\eta} = 0, \quad \theta = 1 \quad \text{on } \eta = \eta_{\min} = 0 \tag{14}$$

$$\psi = \psi_{\xi} = 0, \quad \theta_{\xi} = 0 \quad \text{on } \xi = \xi_{\min} \tag{15}$$

$$\psi_{\eta} = 0, \quad \omega = 0, \quad \theta = 0 \quad \text{as } \eta = \eta_{\max} \tag{16}$$

The conditions on ψ on $\eta = \eta_{\min}$ and $\xi = \xi_{\min}$ correspond to the no-slip condition, while the conditions on ψ and ω given in (16) correspond to the conditions satisfied by the self-similar boundary layer solution and therefore η_{\max} must be sufficiently large to contain the developing disturbances. The thermal boundary conditions correspond to a unit temperature heated surface at $\eta = \eta_{\min}$, a zero ambient temperature and an insulated surface at $\xi = \xi_{\min}$.

In our computations we take $\xi_{\min} = 20$; this means that the corresponding curved surface is nearly horizontal, as displayed in Fig. 1. Given the form of A in Eq. (13) and its presence multiplying the left-hand sides of (11) and (12), the value of ξ_{\min} chosen allows us to use the DuFort–Frankel method to march the solution forward in time. If ξ_{\min} had been chosen to be 0, which corresponds to a second plane surface located at an angle of $2\pi/3$ from the x -axis, then a more difficult and computationally much slower fully implicit method, such as that used by Rees and Bassom [23], would need to be adopted. Although this is a device which simplifies the computational code development, the fact that the flow is advectively unstable, rather than absolutely unstable, suggests that the effect of this slight change in the computational domain is minimal in terms of the results obtained.

As a result of taking $\xi_{\min} = 20$ as the leading edge, the origin of the coordinate system is outside of the fluid domain. In Cartesian coordinates the leading edge is at $y = 0$ and $x = 36.993$, and therefore, for convenience of presentation later, we define the Cartesian variable

$$x^* = x - 36.993 \tag{17}$$

to denote distance from the leading edge of the heated surface.

The boundary conditions at outflow at $\xi = \xi_{\max}$ are discussed at length and given in Section 3.

2.4. Boundary layer approximation

The steady state boundary layer approximation may also be derived from Eqs. (10)–(12) in the following forms

$$\psi_{\eta\eta} = \left(\frac{3}{4}\xi\right)^{2/3} \omega \tag{18}$$

$$\omega_{\eta\eta} + \psi_{\xi}\omega_{\eta} - \psi_{\eta}\omega_{\xi} + \left(\frac{3}{4}\xi\right)^{1/3} \theta_{\eta} = 0 \tag{19}$$

$$Pr^{-1}\theta_{\eta\eta} + \psi_{\xi}\theta_{\eta} - \psi_{\eta}\theta_{\xi} = 0 \tag{20}$$

for which the solution in the new coordinate system is

$$\psi \sim \frac{3}{4}\xi f(\eta), \quad \omega \sim \left(\frac{3}{4}\xi\right)^{1/3} f''(\eta), \quad \theta \sim h(\eta) \tag{21}$$

where f and h satisfy Eqs. (5) and (6).

2.5. Linear disturbance equations

We consider a small disturbance in the steady flow by setting

$$\begin{aligned} \psi(\xi, \eta, t) &= \bar{\psi}(\xi, \eta) + \delta\hat{\psi}(\xi, \eta, t) \\ \theta(\xi, \eta, t) &= \bar{\theta}(\xi, \eta) + \delta\hat{\theta}(\xi, \eta, t) \end{aligned} \tag{22}$$

where δ is asymptotically small, so that powers of δ may be neglected. Here, overbars denote the basic flow variables and hats denote the perturbation variables.

Substituting (22) into Eqs. (10)–(12) and dropping terms which are nonlinear in δ leads to two sets of equations: one for the steady flow and the other for the perturbation flow. The perturbation equations are given by

$$\hat{\psi}_{\xi\xi} + \hat{\psi}_{\eta\eta} = A\hat{\omega} \tag{23}$$

$$A\hat{\omega}_t = \hat{\omega}_{\xi\xi} + \hat{\omega}_{\eta\eta} + \bar{\psi}_{\xi}\hat{\omega}_{\eta} + \bar{\omega}_{\eta}\hat{\psi}_{\xi} - \bar{\psi}_{\eta}\hat{\omega}_{\xi} - \bar{\omega}_{\xi}\hat{\psi}_{\eta} + A^{1/2}\left(\hat{\theta}_{\xi}\sin\frac{1}{4}\phi + \hat{\theta}_{\eta}\cos\frac{1}{4}\phi\right) \tag{24}$$

$$A\hat{\theta}_t = Pr^{-1}(\hat{\theta}_{\xi\xi} + \hat{\theta}_{\eta\eta}) + \bar{\psi}_{\xi}\hat{\theta}_{\eta} + \bar{\theta}_{\eta}\hat{\psi}_{\xi} - \bar{\psi}_{\eta}\hat{\theta}_{\xi} - \bar{\theta}_{\xi}\hat{\psi}_{\eta} \tag{25}$$

and the boundary conditions are

$$\hat{\psi} = \hat{\psi}_{\eta} = 0, \quad \hat{\theta} = 0 \quad \text{on } \eta = \eta_{\min} = 0 \tag{26}$$

$$\hat{\psi} = \hat{\psi}_{\xi} = 0, \quad \hat{\theta}_{\xi} = 0 \quad \text{on } \xi = \xi_{\min} \tag{27}$$

$$\hat{\psi}_{\eta} = 0, \quad \hat{\omega} = 0, \quad \hat{\theta} = 0 \quad \text{as } \eta = \eta_{\max} \tag{28}$$

The general procedure for the solving the perturbation equations is as follows. First, we compute the steady state basic flow satisfying the nonlinear equations (10)–(12). The reason for needing this is that the solution of the boundary layer equations depart quite markedly from the solution of the steady elliptic equations near $\xi = \xi_{\min}$. Then we solve the linearised disturbance equations (23)–(25) for various initial and boundary conditions in order to study the stability characteristics of the boundary layer flow.

3. Numerical method

Finite difference techniques are used to solve the system of nonlinear equations (10)–(12) and the system of linear equations (23)–(25). The time-dependent equations are discretised using second-order accurate central differences in ξ and η , and the DuFort–Frankel method for the time-derivative and diffusion terms. Although the DuFort–Frankel scheme is not of second order accuracy, timestep checks indicate that our solutions are essentially independent of the timestep we used. The Jacobian terms are approximated using the Arakawa [24] formulation which was designed to be particularly suitable for flows which are unstable. Derivative boundary conditions are approximated using a standard fictitious point approach, for although a straightforward first order approximation at a boundary does not destroy overall second order accuracy, the fictitious point method has a smaller absolute error.

The Poisson equation satisfied by the streamfunction was solved using the multigrid Correction Scheme algorithm to accelerate iterative convergence. It incorporates a V-cycling algorithm involving the line Gauss–Seidel relaxation procedure. The method is based on the pointwise method described in Briggs [25], but adopts two line relaxations per coordinate direction on each multigrid level in order to maximise iterative convergence speed.

The conditions to be applied on the outflow boundary follow the methodology introduced by Kloker [26]. The naive imposition of boundary conditions involving either the first or second derivatives of dependent variables result in the progressive upstream propagation of spatially pointwise oscillations which eventually degrade the evolving solution. Kloker et al. [27] discuss at length six different strategies for dealing with outflow conditions and conclude that, for the Blasius boundary layer at least, a very satisfactory method is to use an absorbing buffer region. Such a region is used to damp out disturbances to the basic flow and is sometimes called a relaminarisation region. The method has also been used very satisfactorily in other flows; see Stemmer et al. [28] and Bake et al. [29] for example. For the present problem the concept of a buffer region translates into setting

$$\chi_{\text{DIST}}^{\text{new}} = F(\xi) \times \chi_{\text{DIST}}^{\text{old}} \quad (29)$$

at each timestep. Here χ represents either the vorticity or temperature, χ^{old} is the computed value of χ obtained using the DuFort–Frankel method subject to the boundary condition $\partial\chi/\partial\xi = 0$ at $\xi = \xi_{\text{max}}$, and χ^{new} is the value of χ which is used to compute χ at subsequent timesteps. The buffer function, $F(\xi)$, takes the value, 1, in most of the computational domain, and is a 5th order polynomial in ξ which decreases from 1 at the start of the buffer region to 0 at outflow. At both the beginning ($\xi = \xi_{b1}$) and the end ($\xi = \xi_{b2}$) of the buffer region the function has zero first and second derivatives. In more detail, the buffer function used was

$$F(\xi) = \begin{cases} 1, & \xi < \xi_{b1} \\ 1 - 10\gamma^3 + 15\gamma^4 - 6\gamma^5, & \xi_{b1} < \xi < \xi_{b2} \\ 0, & \xi > \xi_{b2} \end{cases} \quad (30)$$

where

$$\gamma = \frac{\xi - \xi_{b1}}{\xi_{b2} - \xi_{b1}} \quad (31)$$

For nonlinear problems, such as those involving the computation of the basic steady flow, the outflow formula, (29), translates into the following form which is suitable for solving for the true variables, rather than for disturbances,

$$\chi^{\text{new}} = F(\xi) \times \chi^{\text{old}} + [1 - F(\xi)] \times \chi^{\text{basic}} \quad (32)$$

where χ^{basic} represents the basic boundary layer solutions of the corresponding variable (vorticity or temperature) which is obtained from the steady solutions of Eqs. (10)–(12).

In the computation we took $\xi_{\text{max}} = 620$, $\xi_{\text{min}} = 20$, $\eta_{\text{max}} = 12$ and $\eta_{\text{min}} = 0$, with a regular grid of 480 points in the ξ direction and 48 points in the η direction. We have $\delta\xi = 5\delta\eta$ which yields a cell aspect ratio of 5, and therefore a line relaxation method is essential. We were able to take 5 multigrid levels and each V-cycle was comprised of 2 relaxation sweeps in each coordinate direction for each grid. The buffer region extended from the 400th to the 480th point in the ξ direction. At each timestep the vorticity and temperature fields are updated for the new time level, followed by the solution of the Poisson equation for the streamfunction and finally the boundary vorticity is computed using the fictitious point approximation.

When the boundary layer solution as given in Eq. (21) on all grid points is used as the initial condition, the flow evolves rapidly near the leading edge which induces a large thermal wave to form and to propagate downstream. This wave becomes highly nonlinear quite rapidly and very thin internal shear layers develop which are resolved very poorly by the grid we use. Consequently the method becomes numerically unstable and quickly yields temperatures which are outside of the range 0 to 1. Therefore we adopted an ad hoc strategy of removing highly nonlinear disturbances by interpolating both the θ and ω profiles from either side of the nonlinear wave. As the wave had by this time already propagated downstream of the leading edge region in which the wave had been initiated, the resulting modified flow, when integrated forward in time, eventually produces a highly nonlinear wave some distance further downstream. This procedure was continued as often as was necessary to “clean” the boundary layer of unsteady components in order to obtain the steady-state solution of the full equations. The procedure works only because the flow is convectively (or, perhaps less confusingly in the free convection context, advectively) unstable as opposed to being absolutely unstable.

In our numerical computations we discuss two different types of localised disturbance placed near the leading edge. The next section considers the evolution of a disturbance placed within the boundary layer at one point in time. Thereafter attention is focused on unsteady local variations in the boundary temperature in order to determine the detailed effect of different disturbance frequencies.

4. Evolution of an initial disturbance

A disturbance was introduced by setting $\hat{\theta} = 1$ at the point $(\xi, \eta) = (45, 1.5)$, i.e. at $(x, \eta) \simeq (110, 1.5)$, which is fairly

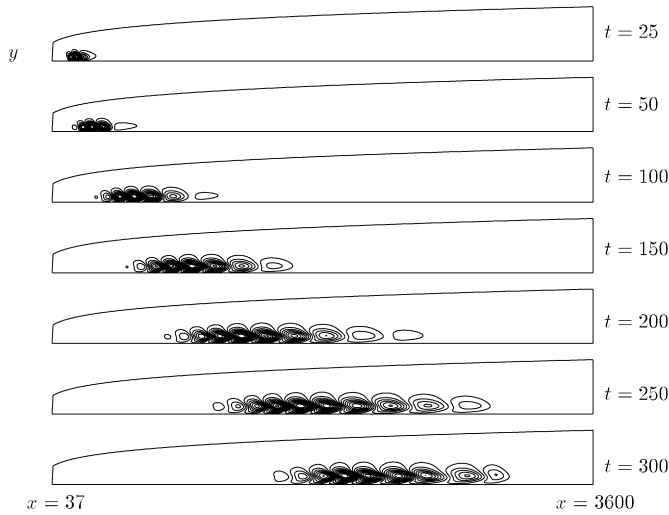


Fig. 2. Contours of $\hat{\theta}$ depicting the response to a point disturbance at $(x, \eta) \simeq (110, 1.5)$, and are scaled to lie within the respective extrema in each frame.

close to the leading edge, and 7000 timesteps of length $\delta t = 0.1$ were used. Although such a point disturbance introduces a checkerboard pattern in the temperature profile at subsequent timesteps, the effect does not last long since the timestep is quite small.

As time progresses the disturbance diffuses outwards from its point of introduction and travels along the boundary layer due to the overall upwards movement of the fluid. The perturbation temperature field in the x – y plane has been recorded at different times from $t = 25$ to $t = 300$ and these are displayed in Fig. 2—it is very important to note that the depicted aspect ratios of the cells are very different from what would be observed in practice since in this figure $x_{\max} \simeq 3500$ and $y_{\max} \simeq 60$. From these contours, both the diffusion and advection of the evolving disturbance are seen clearly with well-defined advancing and trailing edges. The cells at $t = 250$ show a distinctive “boomerang” shape; such a shape arises because the maximum velocity of the basic flow occurs away from the surface. The final frame ($t = 300$) corresponds to a point in time just before the advancing front encounters the buffer region.

Fig. 2 clearly shows the spatial extent of the wavepacket, but also shows how the wavelength of the cells increases with distance from the leading edge. This is consistent with the fact that the basic flow accelerates in the streamwise direction. We note that the train of cells is not spatially periodic.

The variation in the perturbation surface rate of heat transfer, defined by,

$$Q(x, t) = \left. \frac{\partial \hat{\theta}}{\partial \eta} \right|_{\eta=0} \quad (33)$$

is displayed as a contour plot in Fig. 3. The contours shown correspond to plus and minus various powers of 10. The lower boundary of the contours in Fig. 3 shows how quickly the advancing front of the disturbance propagates downstream and, given the decreasing slope, is seen to accelerate. This is consistent with the fact the basic boundary layer flow also accelerates since $u \propto x^{1/2}$. The upper boundary of the contours

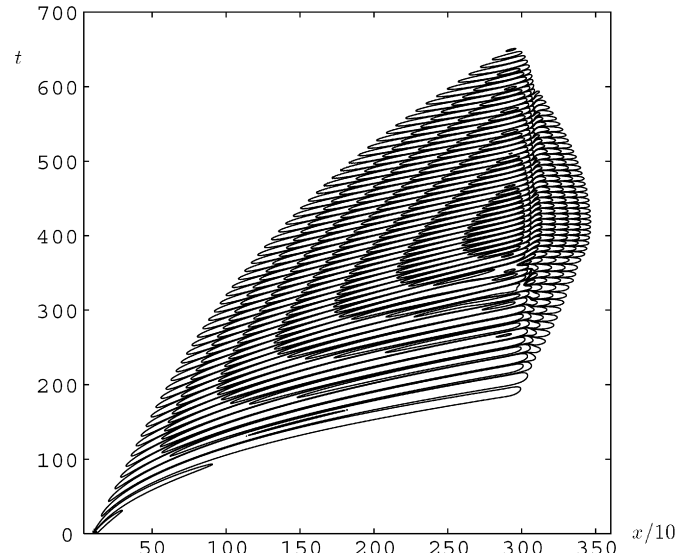


Fig. 3. Variation of $Q(x, t)$ after the introducing the point disturbance.

corresponds to the trailing edge of the wave packet, which also accelerates, and therefore the instability is confirmed as being advective in nature. On the right-hand side the buffer region corresponds to $x > 3000$ and is seen to dampen the disturbances. Although this region appears to have a significant effect on the flow, and indeed this is the intention, it has an almost negligible influence on the region upstream of it. This was tested by using a larger buffer region and comparison of the profiles outside of this larger region showed almost no difference between the two simulations.

The disturbance depicted in Fig. 3 grows rapidly as it travels downstream as evidenced by the fact that the contours at $x \simeq 2800$ and $t \simeq 400$ correspond to a perturbation which is 10^6 stronger than at the depicted trailing edge of the disturbance. It is also interesting to note that there seems to be a distinctive timescale associated with the evolving disturbance; the interval between successive zeros in the perturbation heat transfer may be gauged by the vertical distance between isotherms in Fig. 3.

We have also investigated the effect of changing the location and spatial extent of the initiating disturbance, but the overall qualitative nature of the response of the boundary layer is the same and therefore we have not presented further results—this behaviour was also noted by Janssen and Armfield [30] in their study of convective instabilities in a differentially heated cavity. However, this section provides the context into which may be set certain aspects of the response of the boundary layer to time-periodic disturbances and which are discussed in Section 5.

5. The response to time-periodic disturbances

A time-periodic thermal disturbance was introduced on the heated surface in the region near the leading edge and which is given by

$$\hat{\theta} = e^{-a(\xi - \xi_0)^2} \sin(\lambda t) \quad \text{at } \eta = 0 \quad (34)$$

where λ is the temporal frequency, and ξ_0 is the centre of the disturbance. In addition, $a = 0.1$ is the chosen scaling factor

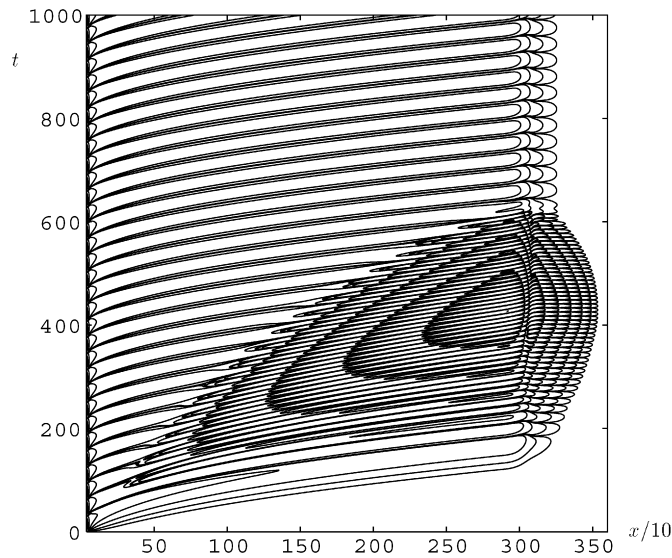


Fig. 4. Variation of $Q(x, t)$ caused by a time-periodic thermal disturbance for $\lambda = 0.1$.

which ensures that the disturbance is well-resolved on the computational grid but also does not get close to the neutral distance.

We used 10,000 timesteps of length $\delta t = 0.1$ in all the computations. In all cases considered this length of time is more than sufficient for transient effects to decay, and for a time-periodic response to be established. We also note that the solutions we present are graphically identical to those obtained using smaller timesteps. Although we are unaware of experimental work which has used time-periodic disturbances to determine the receptivity of external thermal boundary layers in a free convective flow over a vertical heated surface, Liepmann et al. [31] used localised time-periodic heating to generate TS waves into the boundary layer of flow on a horizontal flat plate.

As in the last section, variations in the location, ξ_0 , where the disturbance is centred leads to no significant change in the boundary-layer response. We therefore concentrate on those cases for which $\xi_0 = \xi_{\min} = 20$. In similar fashion, only slight quantitative differences are found when different values of the scaling factor, a , are used, and therefore we concentrate solely on variations in the frequency, λ .

For the frequency, $\lambda = 0.1$, the variation with time of the perturbation surface rate of heat transfer, $Q(x, t)$, is plotted in Fig. 4. The contours in this and subsequent figures of the same type are scaled with respect to the maximum and minimum values of Q in each frame, and successive contour levels are the maximum value of $|Q|$ multiplied by plus and minus successive negative integer powers of 10. The intention is obtain a qualitative feel for the boundary layer response. Although the computations are undertaken in the (ξ, η) coordinate system we present these results in terms of the nondimensional Cartesian coordinate, x .

This figure shows that there are two very different timescales present: (i) a relatively long one which is associated with the forcing timescale and which is most evident at later times, and (ii) a relatively short one which is effectively the start-

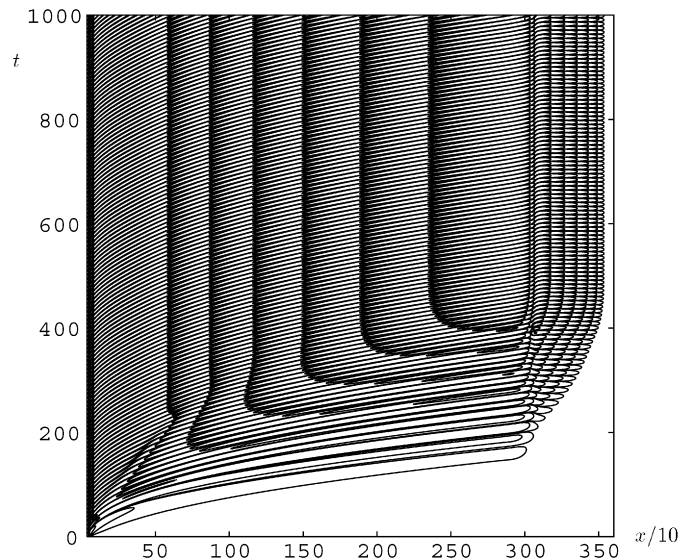


Fig. 5. Variation of $Q(x, t)$ caused by a time-periodic thermal disturbance for $\lambda = 0.4$.

ing transient. Near the point $(x, t) \simeq (300, 100)$ the transient first becomes evident and the contour bands associated with the starting transient are very similar indeed to those of the initial disturbance case which is plotted in Fig. 3.

Once the transient has left the computational domain, the flow after $t \simeq 650$ is essentially time-periodic. The contour spacing for $x > 1000$ does not vary greatly and therefore we may conclude from this evidence that the disturbance is essentially neutral for this value of λ . However the contours indicate that there is clearly fairly strong decay in the region $x < 100$, which is the region where one expects all disturbances to decay since it lies below the neutral stability curve first computed by Nachtsheim [3].

Fig. 5 shows the response when $\lambda = 0.4$. This frequency is roughly the same as that of the transient, and therefore the eventual time-periodic response grows very substantially as it propagates downstream. The magnification in amplitude between $x = 600$ and $x = 2400$ is approximately 10^5 , suggesting that we have what could be interpreted as a resonance between the forcing and the boundary-layer response since this frequency is close to the frequency of the fastest growing mode. This aspect will be dealt with in more quantitative detail below.

The final case we present corresponds to the frequency, $\lambda = 0.55$, and the response returns to the situation where there are two different timescales observed (see Fig. 6). The transient frequency is now smaller than that of the forcing frequency. The region over which the periodic response decays has now increased quite markedly in size, and does so increasingly as λ increases further, although the overall growth which occurs within the computational domain is still substantial. Neutrality appears to be located near $x = 700$. Later we will discuss how this feature is connected with the neutral curve obtained by Paul et al. [17] using the parallel flow approximation. But again we note that the range over which decay takes place increases as λ increases; see Paul [32] for details, which contains further contour plots for different values of $\lambda > 0.55$.

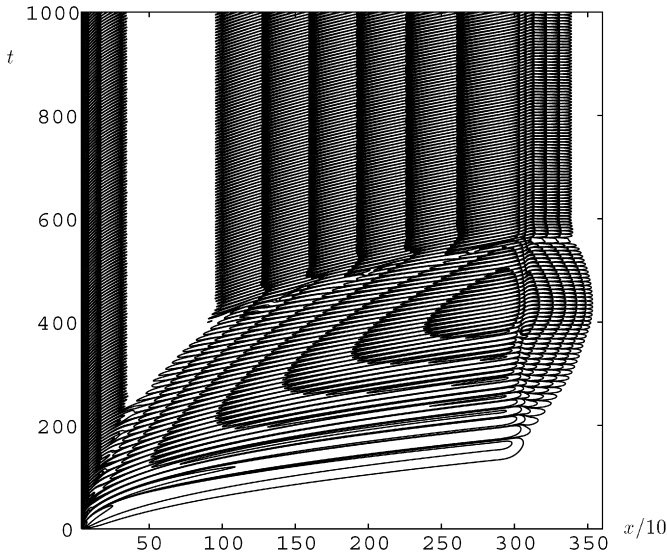


Fig. 6. Variation of $Q(x, t)$ caused by a time-periodic thermal disturbance for $\lambda = 0.55$.

6. Overview of the response to time-periodic disturbances

Fig. 7 summarises Figs. 4–6 in terms of the variation with x of the spatial wavelength of the periodic response. This variation is also shown for many other different values of λ . These results correspond to the final timestep, i.e. for $t = 1000$, as the flow is periodic after $t = 800$. The horizontal coordinate of each circle represents the position, x , of either a maximum or a minimum surface rate of heat transfer, while the vertical coordinate gives the distance between the nearest positions of zero surface heat transfer, i.e. half a “wavelength”, $L/2$. For all values of λ the curves rise with increasing x suggesting that an increasing wavelength with distance is indeed a global feature of the this accelerating boundary layer flow. We also note that the spatial wavelength decreases monotonically with increasing values of the temporal frequency λ . In this regard, slightly anomalous behaviour occurs when $\lambda > 0.55$; this may be traced to the fact that there is an adjustment in the shape of the disturbance near to the point where the heat transfer is smallest, as seen in Fig. 6. This feature persists for higher values of λ (see Paul [32]).

Fig. 8 shows the maximum absolute surface rate of heat transfer over the whole of the heated surface ($37 \leq x \leq 3600$). This quantity is defined by

$$M(\lambda) = \max_{(\xi,t)} \left| \left(\frac{\partial \hat{\theta}}{\partial \eta} \right)_{\eta=0} \right| \tag{35}$$

and is a function of the forcing frequency λ . The curve (a) corresponds to the overall maximum response of the boundary layer, including the transient stage, and in this case M is maximised over $0 \leq t \leq 800$. The curve (b) represents the maximum over one period of the final periodic state. The curves shown in Fig. 8 were obtained by running our simulations for almost 100 different values of λ .

In many cases there is a substantial difference between the maximum transient response and the maximum asymptotic response. This is especially so near $\lambda = 0.3$ and $\lambda = 0.6$. Indeed,

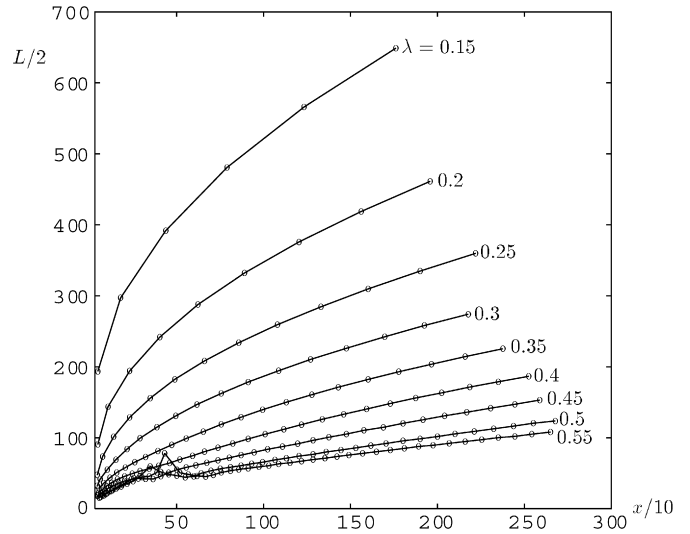


Fig. 7. The variation in the spatial wavelength, L , with distance downstream.

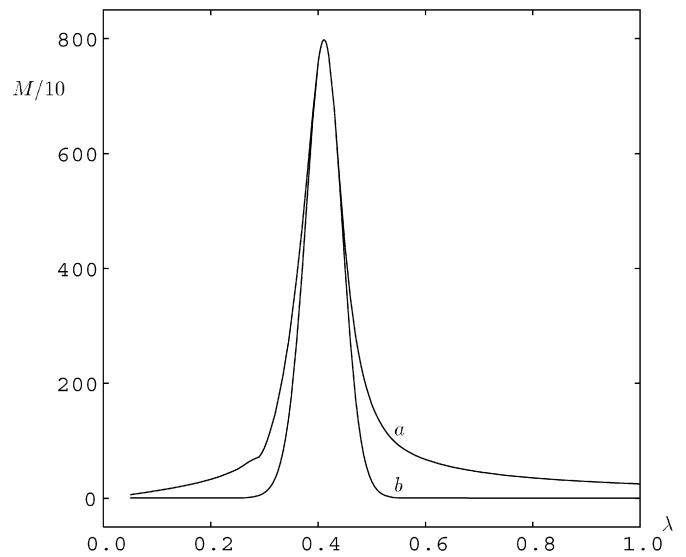


Fig. 8. Variation of the maximum response, M , of the disturbance: (a) the transient response; (b) the periodic response.

for $\lambda < 0.3$ and $\lambda > 0.6$ the maximum asymptotic response is very small compared with those values near to $\lambda = 0.4$. When $\lambda \simeq 0.411$ both maxima take the same value $M \simeq 7981$, which is the strongest response obtainable by this boundary layer and therefore this value of λ constitutes the most dangerous disturbance frequency within the computational domain used. There is also a small range of values of λ near to 0.411 where the maximum transient and asymptotic responses are identical.

However, care must be taken over making absolute statements regarding which excitation frequency is the most dangerous since the computational domain is necessarily finite. That this is so may be gleaned from Fig. 9 which shows how the local maximum asymptotic response of the boundary layer varies with x for various values of λ . Specifically we plot the variation of K against x where

$$K(x, \lambda) = \max_{800 < t < 1000} \log_{10} \left| \left(\frac{\partial \hat{\theta}}{\partial \eta} \right)_{\eta=0} \right| \tag{36}$$

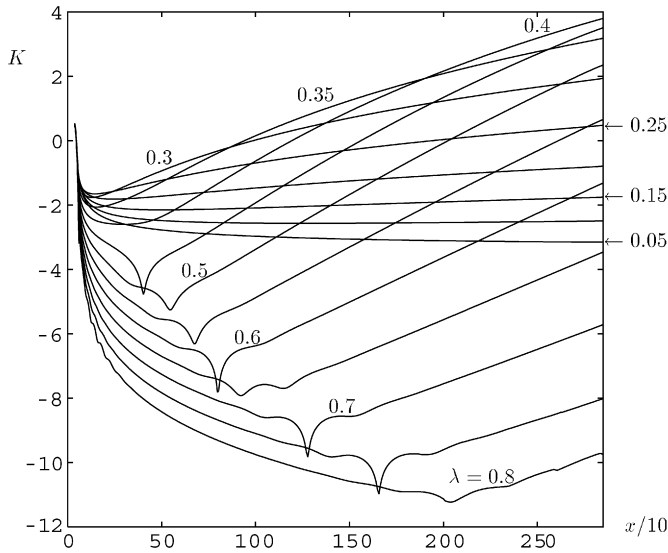


Fig. 9. The variation of $K(\lambda, x)$ with x for various values of the disturbance frequency, λ .

In other words $K(x, \lambda)$ corresponds to the maximum absolute rate of heat transfer over one period at any chosen value of x after transients have died out.

In all cases K decreases rapidly as x increases from $x \simeq 37$, since the leading edge of the heated surface is in a stable region, and therefore all disturbances decay. For the larger values of λ this decay lasts for a considerable distance and the decay is over many orders of magnitude. When $\lambda \geq 0.45$ the K -curves display a sudden dip just before they begin to increase; this is related to the change in the shape of the cell referred to above, and this figure shows that it is a fairly ubiquitous phenomenon. However, when λ takes relatively small values such as 0.05, the disturbance is seen to decay slowly. Our previous comment regarding the near neutrality of the $\lambda = 0.1$ case is borne out by the fact that K hardly varies with x once $x > 1000$.

At intermediate values of λ , such as 0.3, 0.35 and 0.4, we see that the maximum asymptotic response depends on where in the boundary layer one needs the information. For example, at $x \simeq 500$, the most dangerous frequency of excitation, in the sense of yielding the largest response, corresponds roughly to $\lambda = 0.3$. Similarly $\lambda = 0.35$ is the most dangerous frequency when considering the response of the boundary layer at $x \simeq 1300$, whereas $\lambda = 0.4$ corresponds to $x \simeq 2500$. Given the behaviour of the $\lambda = 0.45$ curve we have no reason but expect that it will, in its turn, take over as the most dangerous excitation frequency at a still larger value of x , one which is outside of the present computational domain.

Thus we can depict the upper envelope of the curves shown in Fig. 9 using a sufficiently large number of simulations for different values of λ within the range $0.2 \leq \lambda \leq 0.45$ to summarise the overall boundary layer growth in streamwise direction. The values of λ used to get the upper envelope are shown in Fig. 10 and are denoted by λ_{opt} . Here we see quite clearly how the value of λ_{opt} increases with distance from the leading edge. The minimum value of the envelope occurs at $x^* \simeq 105.5$ (or $x \simeq 142.5$) which is somewhat less than the value $x^* \simeq 147.2$ which is the

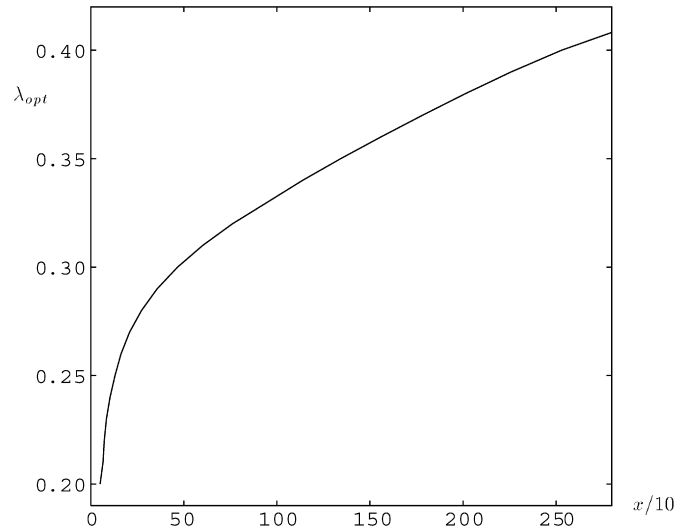


Fig. 10. The values of λ corresponding to the upper envelope of Fig. 9.

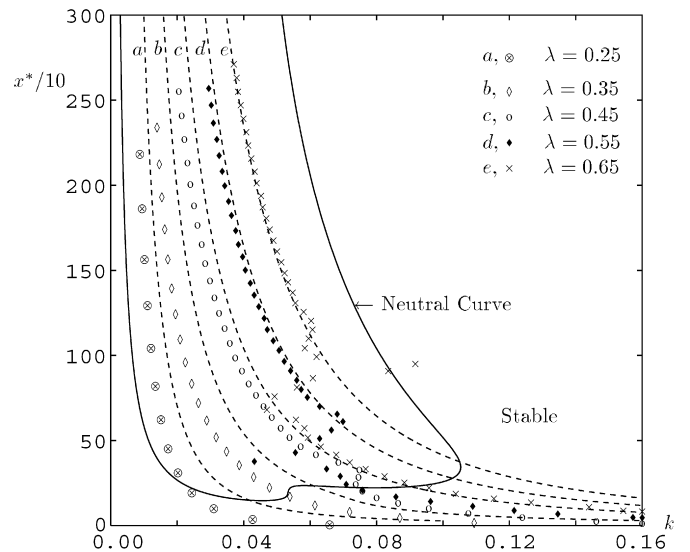


Fig. 11. Comparison between the present elliptic linear stability results and those obtained by assuming the parallel flow approximation. The continuous lines denote the neutral stability curve and dashed lines represent lines of constant frequency. The symbols correspond to fully elliptic results.

minimum value of x^* as given by a straightforward linear stability analysis using the parallel flow approximation (PFA). We shouldn't expect an elliptic analysis and a PFA analysis to yield identical results, and it seems that the stability criterion offered by a PFA is very conservative. However, the corresponding values of λ are very close: here we find that $\lambda_{opt} \simeq 0.252$ while the value obtained from the imaginary part of the exponential growth rate in a PFA analysis at $x^* = 147.2$ is $\lambda = 0.264$.

Finally, we compare in more detail the present results, and those obtained using the standard linear stability theory based upon the PFA. Such a comparison is shown in Fig. 11 for five different values of the excitation frequency. This figure shows (i) the neutral curve for the onset of convection using the PFA as computed by Paul et al. [17]; (ii) curves which correspond to the above values of λ obtained by assuming the PFA, and (iii) the variation with the local wavenumber of the x values at which

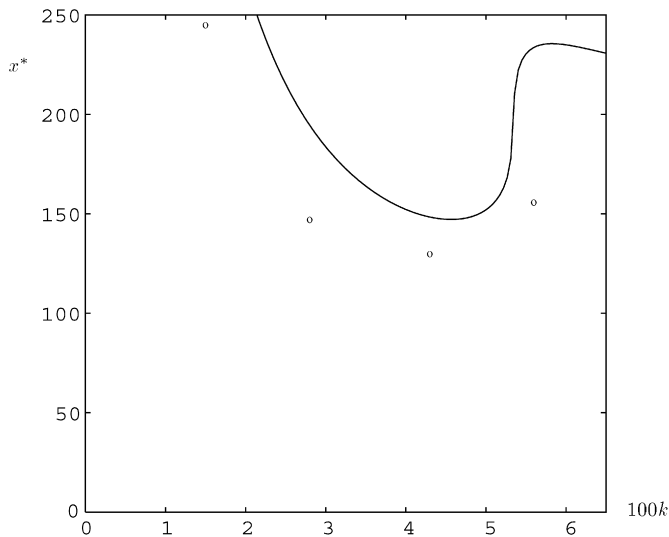


Fig. 12. Comparison between the neutral curves obtained from the parallel flow approximation (solid curve) and the present elliptic linear stability results (circles).

the local perturbation heat transfer is zero at a representative point in time. In this third case the local wavenumber is defined as $k = 2\pi/L$, where the local wavelength L is as depicted in Fig. 7.

When $\lambda = 0.55$ the agreement between the present simulations and the PFA results, shown in Fig. 11 are very good when $x > 750$. Such an agreement is to be expected since PFA data often agree well with data obtained from nonparallel studies when the local wavenumber ($kx^{1/4}$, in this case) is large. At smaller values of x the poor comparison is assumed to be caused partly by the change in the shape of the cells, a phenomenon which is unlikely to occur in the PFA computations which are strictly local, and by the nonparallel and elliptical nature of the flow. As λ decreases from 0.55 the comparison is decreasingly good even at large values of x suggesting that the elliptic effects are so strong that the PFA is no longer a suitable assumption to make. Indeed, this clearly must be the case for relatively small values of x (i.e. those close to the base of the neutral curve) since the spatial wavelength of the resulting cells become comparable to the magnitude as the neutral distance.

Fig. 12 shows a direct comparison between the PFA neutral curve and the interpolated values of x^* and k where neutrality occurs for the present simulations. In this figure we see that the fully elliptic theory yields a stability criterion which is a little more severe than for the PFA. That this is so is not surprising for the PFA imposes restrictions on the disturbance, while the present simulation allows disturbances to evolve freely in both time and space.

7. Conclusions

In this paper we have sought to understand how the classical thermal boundary layer from a heated vertical surface responds to two different types of disturbance, by solving the unsteady, fully elliptic equations of motion, rather than to use approx-

imate methods. Thus the flow has been able to evolve freely in space without having its wavelength prescribed (as with the PFA), or neglecting streamwise diffusion (as with parabolic methods).

We have confirmed numerically that the present boundary layer is advectively, rather than absolutely, unstable, at least within the present computational domain. Given that the basic flow accelerates as it travels upwards, this may possibly imply that absolute instability does not arise. However, we have seen that the upward acceleration does result naturally in a progressive stretching of the individual disturbance cells.

When the boundary layer is subject to harmonic disturbances in time, the strength of the subsequent response depends very highly on the frequency of the disturbance and there appears to be a most dangerous frequency in terms of the strength of the overall response. However, our chief conclusion is that it is not possible to determine a most dangerous disturbance frequency as a global criterion. Rather, each streamwise location in the boundary layer has associated with it its own most dangerous frequency, at least in terms of the heat transfer response to otherwise identical disturbances. We have also seen that this frequency increases with increasing distance, which is the opposite to the conclusion of Brooker et al. [15] who state that the frequency decreases. However, there are significant differences between the two respective studies: the present paper deals with the external flow of air in a uniformly cold environment, while Brooker et al. consider water in a differentially heated square cavity where the core temperature field is stratified.

Finally, although much is known from experimental work about the destabilisation of vortices on inclined surfaces, we are unaware of any published work, except that of Szweczyk [33], which deals with secondary instabilities for vertical free convective flows. Szweczyk found one mechanism for the destabilisation of two-dimensional nonlinear waves which takes the form of a counter-rotating pair of streamwise vortices. The presence of such vortices is unlikely to be connected to those found on inclined surfaces since the latter are thermo-convective in origin, whereas the former take place in the presence of strongly nonlinear waves. A natural extension of this work would be to investigate such three-dimensional secondary instabilities.

Acknowledgements

The first author would like to acknowledge the receipt of an Overseas Research Studentship (ORS) and to thank the University of Bath for postgraduate funding. The authors thank to the anonymous reviewers for their valuable comments and suggestions on the earlier version of this paper, which have served to improve the manuscript.

References

- [1] S.E. Haaland, E.M. Sparrow, Vortex instability of natural convection flow on inclined surfaces, *Int. J. Heat Mass Transfer* 16 (1973) 2355–2367.
- [2] T.S. Chen, K.L. Tzuoo, Vortex instability of free convection flow over horizontal and vertical surfaces, *Trans. ASME J. Heat Transfer* 104 (1982) 637–643.

- [3] P.R. Nachtsheim, Stability of free convection boundary layer flows, Tech. rep., NASA report TN D-2089, 1963.
- [4] C.A. Heiber, B. Gebhart, Stability of vertical natural convection boundary layers, *J. Fluid Mech.* 48 (1971) 625–646.
- [5] M.V. Morkovin, Critically evaluation of transition from laminar to turbulent shear layers with emphasis on hypersonically travelling bodies, Tech. rep., Tech. Rep. AFFDL-TR-68-149, 1969.
- [6] M.E. Goldstein, The evolution of Tollmien–Schlichting waves near a leading edge, *J. Fluid Mech.* 127 (1983) 59–81.
- [7] M.E. Goldstein, Scattering of acoustic waves into Tollmien–Schlichting waves by small streamwise variations in surface geometry, *J. Fluid Mech.* 154 (1985) 509–529.
- [8] A.J. Dietz, Local boundary-layer receptivity to a convected free-stream disturbance, *J. Fluid Mech.* 378 (1999) 291–317.
- [9] X. Wu, Generation of Tollmien–Schlichting waves by convecting gusts interacting with sound, *J. Fluid Mech.* 397 (1999) 285–316.
- [10] X. Wu, Receptivity of boundary layers with distributed roughness to vortical and acoustic disturbances: A second-order asymptotic theory and comparison with experiments, *J. Fluid Mech.* 431 (2001) 91–133.
- [11] X. Wu, On local boundary-layer receptivity to vortical disturbances in the free stream, *J. Fluid Mech.* 449 (2001) 373–393.
- [12] C.K.W. Tam, The excitation of Tollmien–Schlichting waves in low subsonic boundary layers by free-stream sound waves, *J. Fluid Mech.* 109 (1981) 483–501.
- [13] O.M. Haddad, T.C. Corke, Boundary layer receptivity to free-stream sound on parabolic bodies, *J. Fluid Mech.* 368 (1998) 1–26.
- [14] H. Fasel, U. Konzelmann, Non-parallel stability of a flat-plate boundary layer using the complete Navier–Stokes equations, *J. Fluid Mech.* 221 (1990) 331–347.
- [15] A.M.H. Brooker, J.C. Patterson, S.W. Armfield, Non-parallel linear stability analysis of the vertical boundary layer in a differentially heated cavity, *J. Fluid Mech.* 352 (1997) 265–281.
- [16] H. Herwig, X. You, Thermal receptivity of unstable laminar flow with heat transfer, *Int. J. Heat Mass Transfer* 17 (1997) 4095–4103.
- [17] M.C. Paul, D.A.S. Rees, M. Wilson, The influence of higher order effects on the linear wave instability of vertical free convective boundary layer flow, *Int. J. Heat Mass Transfer* 48 (2005) 809–817.
- [18] J. Tao, P. Le Quéré, S. Xin, Spatial-temporal instability of the natural convective boundary layer in thermally stratified medium, *J. Fluid Mech.* 518 (2004) 363–379.
- [19] D.A.S. Rees, Vortex instability from a near-vertical heated surface in a porous medium. I. Linear theory, *Proc. Roy. Soc. A* 457 (2001) 1721–1734.
- [20] D.A.S. Rees, Vortex instability from a near-vertical heated surface in a porous medium. II. Nonlinear evolution, *Proc. Roy. Soc. A* 458 (2002) 1575–1592.
- [21] E. Pohlhausen, Der wärmeaustausch zwischen festen körpern und flüssigkeiten mit kleiner wärmeleitung, *Zeitschrift für angewandte Mathematik und Mechanik* 457 (1921) 1721–1734.
- [22] S. Ostrach, An analysis of laminar free-convection flow and heat transfer about a flat plate parallel to the direction of the generating body force, Tech. rep., NACA Report 1111, 1953.
- [23] D.A.S. Rees, A.P. Bassom, The nonlinear nonparallel wave instability of boundary layer flow induced by a horizontal heated surface in porous media, *J. Fluid Mech.* 253 (1993) 267–296.
- [24] A. Arakawa, Computational design of long-term numerical integration of the equations of fluid motion: I. Two dimensional incompressible flow, *J. Comp. Phys.* 1 (1966) 119–143.
- [25] W.L. Briggs, *A Multigrid Tutorial*, Lancaster Press, 1987.
- [26] M. Kloker, Direkte numerische simulation des laminar-turbulenten umschlages in einer stark verzögerten grenzschicht, Ph.D. thesis, Institut für Aerodynamik und Gasdynamik, Stuttgart, 1993.
- [27] M. Kloker, U. Konzelmann, H. Fasel, Outflow boundary conditions for spatial Navier–Stokes simulations of transitional boundary layers, *AIAA J.* 31 (1993) 620–628.
- [28] C. Stemmer, M.J. Kloker, S. Wagner, Navier–Stokes simulation of harmonic point disturbances in an airfoil boundary layer, *AIAA J.* 38 (2000) 1369–1376.
- [29] S. Bake, G.W. Meyer, U. Rist, Turbulence mechanism in Klebanoff transition: a quantitative comparison of experiment and direct numerical simulation, *J. Fluid Mech.* 459 (2002) 217–243.
- [30] R. Janssen, S. Armfield, Stability properties of the vertical boundary layers in differentially heated cavities, *Int. J. Heat Fluid Flow* 17 (1996) 547–556.
- [31] H.W. Liepmann, G.L. Brown, D.M. Nosenchuck, Control of laminar-instability waves using a new technique, *J. Fluid Mech.* 118 (1982) 187–200.
- [32] M.C. Paul, The stability of free convective boundary layer flows, Ph.D. thesis, University of Bath, UK, 2002.
- [33] A.A. Szewczyk, Stability and transition of the free-convection layer along a flat plate, *Int. J. Heat Mass Transfer* 5 (1962) 903–914.